Enhanced Natural Releases of Mercury in Response to Reduction of Anthropogenic Emissions during the COVID-19 Lockdown by Explainable Machine Learning

Xiaofei Qin[1], Shengqian Zhou[1], Hao Li[1], Guochen Wang[1], Cheng Chen[1], Chengfeng Liu[1], Xiaohao Wang[2], Juntao Huo[2], Yanfen Lin[2], Jia Chen[2], Qingyan Fu[2], Yusen Duan[2], Kan Huang[1,3,4*], Congrui Deng[1*]

[1]Center for Atmospheric Chemistry Study, Shanghai Key Laboratory of Atmospheric Particle Pollution and Prevention (LAP3), Department of Environmental Science and Engineering, Fudan University, Shanghai, 200433, China

[2]State Ecologic Environmental Scientific Observation and Research Station for Dianshan Lake, Shanghai Environmental Monitoring Center, Shanghai, 200030, China

[3]Institute of Eco-Chongming (IEC), Shanghai, 202162, China

[4]IRDR ICoE on Risk Interconnectivity and Governance on Weather/Climate Extremes Impact and Public Health, Fudan University, Shanghai 200433, China

Corresponding authors: huangkan@fudan.edu.cn; congruideng@fudan.edu.cn

Abstract. The widespread of coronavirus (COVID-19) has significantly impacted the global human activities. Compared to numerous studies on conventional air pollutants, atmospheric mercury that has matched sources from both anthropogenic and natural emissions is rarely investigated. At a regional site in Eastern China, an intensive measurement was performed, showing obvious decreases of gaseous elemental mercury (GEM) during the COVID-19 lockdown, while not as significant as most of the other measured air pollutants. Before the lockdown when anthropogenic emissions dominated, GEM showed no correlation with temperature and negative correlations with wind speed and the height of boundary layer. In contrast, GEM showed significant correlation with temperature while the relationship between GEM and wind speed/boundary layer disappeared during the lockdown, suggesting the enhanced natural emissions of mercury. By applying a machine learning model and the Shapley Additive ExPlanation Approach, it was found that the mercury

pollution episodes before the lockdown were driven by anthropogenic sources, while they were mainly driven by natural sources during and after the lockdown. Source apportionment results showed that the absolute contribution of natural surface emissions to GEM unexpectedly increased (44%) during the lockdown. Throughout the whole study period, a significant negative correlation was observed between the absolute contribution of natural and anthropogenic sources to GEM. We conclude that natural release of mercury could be stimulated to compensate the significantly reduced anthropogenic GEM via the surface - air exchange balance of mercury.

Keywords: gaseous elemental mercury, lockdown, correlation, explainable machine learning, natural mercury

1 Introduction

Mercury pollution has received widespread attention due to its long-range transport, bioaccumulation, and neurotoxicity (Giang and Selin, 2016; Horowitz et al., 2017; Driscoll et al., 2013). The atmosphere is the key to the distribution of mercury on the global scale, because gaseous elemental mercury (the predominant form of mercury in the atmosphere, >90%) has relatively high stability and long residence time, and can be transported through the atmosphere for long distances (Xu et al., 2017; Mao et al., 2016). Mercury in the atmosphere derives from both anthropogenic emissions and natural processes. The main anthropogenic sources of atmospheric mercury include coal combustion, nonferrous smelters, cement production, waste incineration, and mining (Wu et al., 2018; Wu et al., 2016). The amount of mercury in the atmosphere directly emitted by anthropogenic activities accounted for about 30% of global mercury emissions (Streets et al., 2019; Steenhuisen and Wilson, 2019) and China is the country with the largest anthropogenic atmospheric mercury emissions in the world (Liu et al., 2019). The natural sources of mercury in the atmosphere are mainly from the exchange processes between natural surfaces (e.g., soil, vegetation, and water) and the atmosphere (Outridge et al., 2018; Pirrone et al., 2010). Unlike anthropogenic emissions, natural releases of mercury are passive emissions and are susceptible to various environmental factors, such as meteorological parameters (e.g., solar radiation, temperature, and atmospheric turbulence), surface properties (e.g., soil/water mercury content, organic matter, and microbial activity), and ambient air characteristics (e.g., Hg^0 concentration and O_3 concentration in the

atmosphere) (Zhu et al., 2016). Previous studies have focused on the effects of various meteorological factors and different medium properties on natural surface releases of mercury. The soil Hg^0 flux and solar radiation showed a high positive correlation, which was generally considered that high solar radiation tended to promote the reduction of Hg^{II} to Hg^0 (Carpi and Lindberg, 1997; Poissant et al., 2004; Bahlmann et al., 2006). High wind speed was conductive to the release of mercury from seawater (Wanninkhof, 2014). The terrestrial vegetations acted as a global mercury pump (Jiskra et al., 2018) and deforestation would increase forest floor radiation and temperature, thereby increasing Hg^0 emissions (Carpi et al., 2014; Mazur et al., 2014). However, few studies have investigated the impact of changes in ambient GEM concentration in response to the natural surface emissions of Hg^0. Under the background that the global Hg^0 concentration has been decreasing year by year (Zhang et al., 2016b), it is particularly urgent and important to conduct such research.

China has taken many stringent and ambitious control measures since 2013 to tackle the severe air pollution, such as imposing ultra-low emission standards on coal-fired power plants, and phasing out small and high-emission factories (Zheng et al., 2018). These pollution control measures co-benefited the significant reduction of anthropogenic mercury emissions (Wen et al., 2020; Liu et al., 2018). The anthropogenic atmospheric mercury emissions of China fell by 22% from 2013 to 2017 (Liu et al., 2019) and correspondingly, decreasing trends in the annual mean atmospheric mercury concentration were observed at both Chinese urban and remote sites (Qin et al., 2020; Tang et al., 2018; Yin et al., 2018). In this regard, this change could be likely to affect the surface – air exchange balance of mercury. In the early 2020, China's lockdown measures to control the spread of the 2019 Novel Coronavirus (COVID-19) resulted in a significant reduction in the emissions of primary air pollutants (Chang et al., 2020). One study in the Beijing – Tianjin – Hebei region showed that the anthropogenic emission of atmospheric mercury reduced by about 22% during the lockdown compared with that before the lockdown (Wu et al., 2021). Therefore, the COVID-19 lockdown provided a natural experiment to explore how the natural surface emissions of mercury would respond to the dramatic reduction of anthropogenic mercury emissions. Traditionally, chemical transport models were the most widely used tools for disentangling the contributions from meteorology and various emission sources, while the performance of these models relied heavily on

3

the availability of updated emission inventories with high accuracy (Selin et al., 2007; Holmes et al., 2010; Huang and Zhang, 2021). Therefore, applying traditional models to reproduce and explain some special events and processes of atmospheric mercury could be limited by certain uncertainties. Recently, data-driven methods such as machine learning has been widely used in atmospheric science research (Grange et al., 2018; Vu et al., 2019; Qi et al., 2019). The model performance of machine learning in predicting atmospheric pollutants (such as $PM_{2.5}$) was generally better than traditional chemical transport models (Hou et al., 2022; Yang et al., 2021), however, these results were less robust in terms of interpretability due to the "black box" nature of machine learning model. With the development of data analysis methods, tools that can unlock the mystery of machine learning has been emerging, such as the SHapley Additive exPlanation (SHAP) approach (Stirnberg et al., 2021). Therefore, combined with new interpretation methods, machine learning can be a promising alternative to study the behavior of pollutants in the atmosphere. However, few studies have applied machine learning to the study of atmospheric mercury.

Many receptor - based models have been used to determine the sources and processes of air pollutants, among which the positive matrix factorization (PMF) is a commonly used method (Yu et al., 2019; Sun et al., 2016; Chang et al., 2018). The PMF method provides quantitative source profiles and source contributions, and the obtained source profiles can aid factor interpretation (Belis et al., 2013). Another strength of PMF is that the measurement uncertainty is included in the PMF model, which ensures that species with large uncertainties have less impact on the model results (Hopke, 2016). Many previous studies have applied the PMF method to the source apportionment of atmospheric mercury. One study in Canada compared the PMF model performance of atmospheric mercury in different years and found that the source profiles and source contributions of GEM in 2009 and 2010 were in good agreement (Xu et al., 2017). By using the PMF model, the research on the western coast of Ireland found that baseline and combustion processes were the controlling sources of atmospheric mercury (Custodio et al., 2020). The study in the Yangtze River Delta in eastern China suggested that the contribution of natural sources to GEM had gradually exceeded that of anthropogenic sources from 2015 to 2018 by using the PMF method (Qin et al., 2020). This indicated that it is feasible to use the PMF model to identify the sources of GEM in the atmosphere.

In this study, we first compared the concentration of GEM and its relationship with environmental factors before, during, and after the COVID-19 lockdown. Observational evidence on the changes of anthropogenic and natural sources of GEM was revealed. Then the drivers of the GEM variation throughout the study period were explored by using the machine learning model and explained by a game theoretic approach. Finally, we applied a receptor model to quantify the contribution of anthropogenic and natural sources to GEM and unveiled the response of natural releases of mercury to the reduction of anthropogenic mercury emissions.

2 Materials and Methods

2.1 Site and Instrumentation

Field measurements were conducted at the Dianshan Lake site (31.096°N, 120.988°E; 14 m a.g.l) at the junction of Shanghai, Zhejiang, and Jiangsu provinces of the Yangtze River Delta (YRD) region of China (Figure S1). It represents a rural setting and regional-scale air pollution characteristics of the YRD region. A detailed description of the site can be found in our previous works (Qin et al., 2019; Qin et al., 2020).

Ambient GEM concentration was measured by an automated mercury vapor analyzer (Tekran 2537B/1130/1135 system, Tekran Inc., Canada) at 5-min time resolution, more details of this instrument can be found elsewhere (Qin et al., 2019). Water soluble ions in $PM_{2.5}$ (SO_4^{2-}, NO_3^-, NH_4^+, Cl^-, Na^+, K^+, Mg^{2+}, and Ca^{2+}) and water soluble gases (NH_3 and SO_2) were continuously measured by Monitor for AeRosols and Gases in ambient Air (MARGA) at a flow rate of 16.7 L/min with a time resolution of 1 h (Wang et al., 2022b; Xu et al., 2020). Heavy metals in $PM_{2.5}$ (Pb, Fe, Ba, Cr, Se, Cd, Ag, Ca, Mn, Cu, As, Ni, Zn, and V) were determined hourly by a multi-metal monitor (Xact^{TM} 625; Cooper Environmental, USA) (Wang et al., 2022a). Black carbon in $PM_{2.5}$ were continuously measured by a multi-wavelength Aethalometer (AE-33, Magee Scientific, USA) (Li et al., 2021). Organic carbon (OC) and elemental carbon (EC) in $PM_{2.5}$ were measured by an in situ Semi-Continuous Organic Carbon and Elemental Carbon aerosol analyzer (RT-3195, Sunset Laboratory, Beaverton, Oregon, USA) (Xu et al., 2018). SO_2, CO, O_3, and $PM_{2.5}$ were determined by Thermo Fisher 43i, Thermo Fisher 48i-TLE, Thermo Fisher 49i, and Thermo Fisher 1405-F, respectively. Meteorological parameters including air temperature, relative humidity, wind speed,

146 and wind direction were collected by using a series of Vaisala weather sensors (WXT530 Weather

147 Transmitter Series; Vaisala; Vantaa, Finland) with a time resolution of 10 min.

148 The air pollutants including CO, NO_2, and $PM_{2.5}$ at other ground monitoring stations in the YRD

149 region were obtained from the public database of China National Environmental Monitoring Centre.

150 The data of planetary boundary layer (PBL) height were obtained from the US National Oceanic

151 and Atmospheric Administration (https://www.ready.noaa.gov/archives.php, last access: 31

152 August, 2022). The 3-days air mass backward trajectories were calculated by applying the Hybrid

153 Single Particle Lagrangian Integrated Trajectory (HYSPLIT) model

154 (https://www.ready.noaa.gov/HYSPLIT.php, last access: 31 August, 2022), the MeteoInfo

155 software was used to perform cluster analysis of backward trajectories.

156

2.2 Machine Learning Model

158 The artificial neural network (ANN) model was used to simulate the GEM concentration at the DSL

159 site during the study period. Artificial neural network is a mathematical model based on the basic

160 principles of neural networks in biology. The network structure consists of input layer, hidden layer,

161 and output layer of neurons. The process of obtaining an ANN model is that the neurons of input

162 layer pass through each hidden layer and then reach the output layer. If the expected results are not

163 obtained in the output layer, the errors are propagated back and the neuron weights of each hidden

164 layer are iteratively updated to minimize them. In this study, long-term observational air pollutants

165 (SO_2, CO, O_3, NO_2, and $PM_{2.5}$) and meteorological data (air temperature, relative humidity, and

166 wind speed) in Shanghai from March 1, 2015 to February 28, 2019 were chosen as input variables

167 for training. These variables were directly or indirectly related to the emissions (both anthropogenic

168 and natural sources), transport, and removal processes of GEM. For example, the main sources of

169 SO_2, CO, and NO_2 were fossil fuel combustions, which were also the largest anthropogenic sources

170 of GEM (Zhang et al., 2016a; Streets et al., 2011). The natural sources of GEM were mainly from

171 the release of land and sea surfaces, which were closely related to temperature, relative humidity,

172 and wind speed (Wang et al., 2014; Moore and Carpi, 2005).

173 The detailed training and validation of this model can be found in our previous study (Qin et al.,

174 2022). We have established an ANN model through training the long-term observational data of

175 GEM and other auxiliary environmental parameters at DSL. The long-term observational GEM

176 (hourly data from March 1, 2015 to February 28, 2019; n = 17532) in Shanghai was the target

177 variable for training, and the corresponding air pollutants (SO_2, CO, O_3, NO_2, and $PM_{2.5}$) and

178 meteorological data (air temperature, relative humidity, and wind speed) were chosen as input

179 variables for training. The datasets were randomly divided into three parts, i.e., 70% for training,

180 15% for validation, and 15% for testing. We chose the neural network containing a hidden layer

181 with 20 nodes, and the training algorithm was the Levenberg-Marquardt. The performance of the

182 model was evaluated with the mean square error (MSE) and correlation coefficient (R^2 value). To

183 verify the accuracy of the trained neural network model, we compared the observed (not included

184 in the training data set) and simulated GEM concentrations of DSL from January 1 to February 26,

185 2020, and found that they exhibited a reasonably good correlation with the correlation coefficient

186 (R^2) of 0.67. To test the applicability of the model on the regional scale, we compared the observed

187 and simulated GEM concentrations in Suzhou, Ningbo, Nanjing, and Hefei (Figure S2). In Nanjing

188 and Suzhou, the observed and simulated daily GEM showed consistence with R^2 values of 0.52 and

189 0.71, respectively. In Ningbo, the observed and simulated GEM in summer and winter also showed

190 consistence with R^2 values of 0.64 and 0.65, respectively. A low bias was derived between the

191 observed and simulated seasonal GEM in Hefei. This suggested that it was feasible to use the trained

192 ANN model to simulated the GEM concentrations in Shanghai and even the Yangtze River Delta

193 region.

194

195 **2.3 Shapley Additive ExPlanation (SHAP) Approach**

196 The SHAP approach was applied in this study to explain the ANN model simulation results. This

197 approach constructs a distribution scheme based on coalitional game theory that comprehensively

198 considers the requirements of the conflicting parties, so as to ensure the fairness of the distribution

199 (Lundberg et al., 2018; Lundberg et al., 2020; Hou et al., 2022). In the game theory, the Shapley

200 value of a player represents the average contribution of the player in a cooperative game, which is

201 a fair distribution of the total gain generated by individual players (Lundberg and Lee, 2017b). In

202 the context of machine learning prediction, the Shapley value of a feature at a query point represents

203 the contribution of that feature to the prediction (response for regression or score of each class for

204 classification) at a particular query point (Aas et al., 2021). The Shapley value corresponds to the

205 deviation between the prediction for the query point and the average prediction caused by the feature,

206 and the sum of the Shapley values for all features for specific query point corresponds to the total

207 deviation of the prediction from the average (Kumar et al., 2020). The Shapley value of the ith

208 feature for the query point x is defined by the value function v:

209
$$\varphi_i(v_x) = \frac{1}{N}\sum_{S\subseteq\omega\setminus\{i\}}\frac{\frac{v_x(S\cup\{i\})-v_x(S)}{(N-1)!}}{|S|!(N-|S|-1)!}$$
(1)

210 Where N is the number of all features, ω is the set of all features, $|S|$ is the cardinality of the set

211 S, or the number of elements in the set S, v_x is the value function of the features in a set S for the

212 query point x. The value of the function indicates the expected contribution of the features in S to

213 the prediction for the query point x.

214

215 **2.4 Positive Matrix Factorization (PMF)**

216 The PMF model has proven to be a useful tool for obtaining source profiles and quantifying source

217 contributions of complex air pollution (Gibson et al., 2015). The basic principle of PMF is that the

218 concentration of the sample is determined by the source profiles with different contributions, which

219 can be described as follows.

220
$$X_{ij} = \sum_{k=1}^{P} g_{ik} f_{kj} + e_{ij}$$
(2)

221 where X_{ij} represents the concentration of the jth species in the ith sample, g_{ik} is the contribution of

222 the kth factor in the ith sample, f_{kj} provides the information about the mass fraction of the jth species

223 in the kth factor, e_{ij} is the residual for specific measurement, and P represents the number of factors.

224 The number of factors being from three to eight was explored with the optimal solutions determined

225 by the slope of the Q value versus the number of factors. The Q value is the sum of the square of

226 the difference between the measured and modeled concentrations weighted by the concentration

227 uncertainties, and needs to be minimized before the PMF modeled determines the optimal

228 nonnegative factor profiles and contributions (Cheng et al., 2015).

229
$$Q = \sum_{i=1}^{n}\sum_{j=1}^{m}\left(\frac{X_{ij} - \sum_{k=1}^{p} A_{ik}F_{kj}}{S_{ij}}\right)^2$$

230 Where X_{ij} represents the concentration of the jth contamination in the ith sample, m is the total
231 number of the pollutants, and n is the total number of samples. A_{ik} represents the contribution of the
232 kth factor on the ith sample, and F_{kj} represents the mass fraction of the j pollutant in the kth factor.

8

233 S_{ij} is the uncertainty in the jth pollutant on the ith factor, and P is the number of factors. For each
234 run in this study, the stability and reliability of the outputs were assessed by referring to the Q value,
235 residual analysis, and correlation coefficients between observed and predicted concentrations.
236 Finally, we found that a six-factor solution showed the most stable results and gave the most
237 reasonable interpretation. Detailed description can be seen in previous studies (Qin et al., 2020; Qin
238 et al., 2019).

239

240 **3 Results and Discussion**

241 **3.1 Changes in GEM Concentrations during the Lockdown**

242 Figure 1 shows the time series of hourly GEM concentrations during 1 January to 26 February, 2020.

243 Three periods were defined, i.e., 1 January to 23 January before the lockdown, 24 January to 14

244 February during the lockdown, and 15 February to 26 February after the lockdown. Before the

245 lockdown, hourly GEM showed strong fluctuations with frequent extreme concentrations higher

246 than 5 ng/m^3. In contrast, the diurnal variation of GEM was significantly weakened with hourly

247 concentrations all lower than 4 ng/m^3 during the lockdown. After the lockdown, GEM concentration

248 was slightly higher than that of during the lockdown. On average, GEM declined sharply from 2.78

249 ng/m^3 before the lockdown to 2.06 ng/m^3 during the lockdown, and then rose slightly to 2.26 ng/m^3

250 after the lockdown. Figure 1 also shows typical gaseous pollutants such as sulfur dioxide (SO$_2$),

251 nitrogen dioxide (NO$_2$), and carbon monoxide (CO) behaved similarly as GEM, as well as for PM$_{2.5}$

252 and its components such as black carbon (BC), elemental carbon (EC), lead (Pb), and arsenic (As).

253 This temporal pattern was expected, as the nationwide reduction of automotive mobility and energy

254 consumption due to the COVID-19 lockdown would certainly lead to drops in primary pollutants

255 emissions. As shown in Figure S3, the levels of CO, NO$_2$, and PM$_{2.5}$ in the Yangtze River Delta

256 (YRD) declined sharply during the lockdown by 26%, 61%, and 27%, respectively, which was

257 consistent with emissions estimates based on up-to-date activity levels in eastern China (Huang et

258 al., 2021). For anthropogenic Hg emissions, one study in the Beijing – Tianjin – Hebei region

259 estimated a decline of approximate 22% during the lockdown, which was mainly due to the

260 reduction of cement clinker production, coal-fired power plants, and residential coal combustion

261 (Wu et al., 2021). We compared the meteorological factors (including air temperature, wind speed,

262 relative humidity, and planetary boundary layer height) before, during, and after the lockdown

263 (Table S1). No significant changes of the meteorological factors were observed before and during

the lockdown. In addition, the 3-days backward trajectory cluster analysis indicated that the transport patterns differed little between these two periods (Figure S4). This suggested that the significant decline in GEM concentrations during the lockdown was mainly due to the reduced mercury emissions, rather than changes of synoptic conditions.
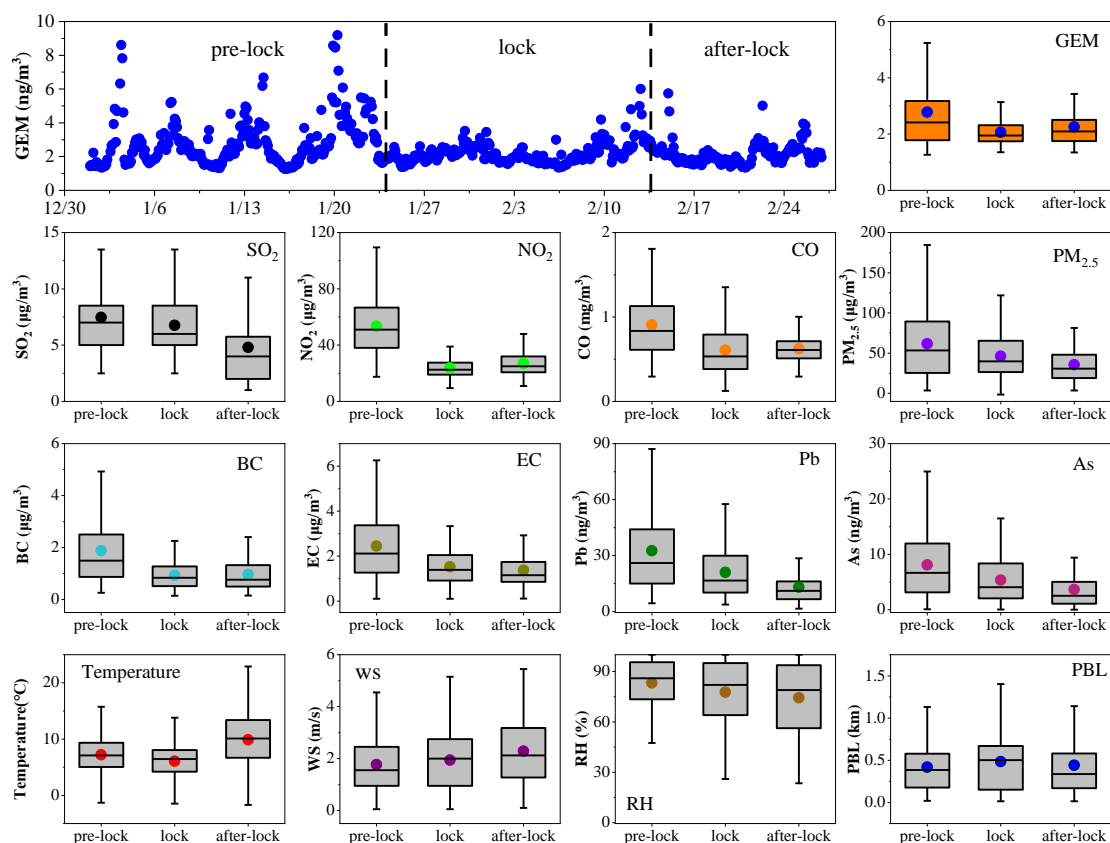
Figure 1. Hourly variations of GEM concentrations from 1 January to 26 February, 2020. Box plots of GEM, SO_2, NO_2, CO, $PM_{2.5}$, BC, EC, Pb, As, and meteorological parameters (temperature, wind speed, relative humidity, and planetary boundary layer height) before, during, and after the lockdown are also shown.

## 3.2 Observational Evidences of Enhanced Effects of Natural Sources on GEM

Table S2 further shows the reduction rates of gaseous pollutants SO_2, NO_2, NO, and CO during the lockdown were 9%, 56%, 64%, and 33%, respectively, compared to those before the lockdown. While O_3 showed almost one-fold increase due to the strongly depressed titration effect from substantial reduced NOx emissions during the lockdown (Huang et al., 2021; Yang et al., 2021). As

for the primary trace elements such as Pb, Fe, Cr, Se, Ca, Mn, As, Ni, and Zn, their reduction rates

ranged from 34% - 73%. As for the main chemical components in $PM_{2.5}$, NO_3^-, NH_4^+, and BC were

strongly reduced by 58%, 45%, and 51%, while SO_4^{2-} and OC were less reduced by 20% and 16%,

respectively. Except for SO_2, SO_4^{2-}, and OC, GEM presented lower reduction rate than the other air

pollutants, probably indicating the discrepancy in key sources for different air pollutants. In order

to probe the dynamic variation of GEM sources across the observational period, we first investigated

the correlations among GEM and main components of $PM_{2.5}$ and gaseous pollutants (Figure 2a).

GEM was found significantly correlated with the primary air pollutants such as CO, K^+, BC, and

EC with the correlation coefficients (R) above 0.7. This suggested that the main anthropogenic

sources of GEM might be coal combustion and biomass burning in Shanghai, which was consistent

with the previous studies in the Yangtze River Delta (Qin et al., 2019; Tang et al., 2018).

BC, EC, and CO are mainly from fossil fuels combustion and biomass burning, and can be

used as indicators of the main anthropogenic sources of GEM. In order to explore the changes in

the sources of GEM, we further investigated the relationship between GEM and BC/EC/CO before,

during, and after the lockdown. As shown in Figure 2, R between GEM and BC, GEM and CO,

GEM and EC during and after the lockdown were lower than that before the lockdown, suggesting

the influence of anthropogenic sources on GEM was weakened during the lockdown. Different from

BC, CO, and EC that are overwhelmingly derived from anthropogenic sources, natural sources such

as surface emission and ocean release also contribute significantly to GEM (Obrist et al., 2018).

Hence, the ratio of GEM/BC, GEM/CO, and GEM/EC can be simply applied as indicators to reveal

the relative importance of anthropogenic versus natural sources. A higher GEM/BC, GEM/CO, and

GEM/EC ratio indicated the more importance of natural sources, and vice versa. As shown in Figure

2k-m, the GEM/BC ratio significantly increased from 1.9×10^{-3} before the lockdown to 3.2×10^{-3}

during the lockdown, the GEM/CO ratio significantly increased from 3.1×10^{-6} to 4.0×10^{-6}, and the

GEM/EC ratio significantly increased from 1.4×10^{-3} to 2.2×10^{-3}. The GEM/CO ratio has been used

to analyze the sources of GEM in many studies. In this study, the GEM/CO ratio during the

lockdown period was 4.0×10^{-6}, which was significantly higher than the anthropogenic GEM/CO

emission ratio in mainland China, South Asia, and Indochinese Peninsula, whose values were 2.7,

2.6, and 1.5×10^{-6}, respectively (Fu et al., 2015), also higher than the GEM/CO ratio observed in

Nanjing (3.1×10^{-6}) and Beijing (1.5×10^{-6}) in winter (Zhang et al., 2013; Zhu et al., 2012).This corroborated that the impact of natural sources on GEM could be more outstanding during the lockdown than before and after the lockdown.
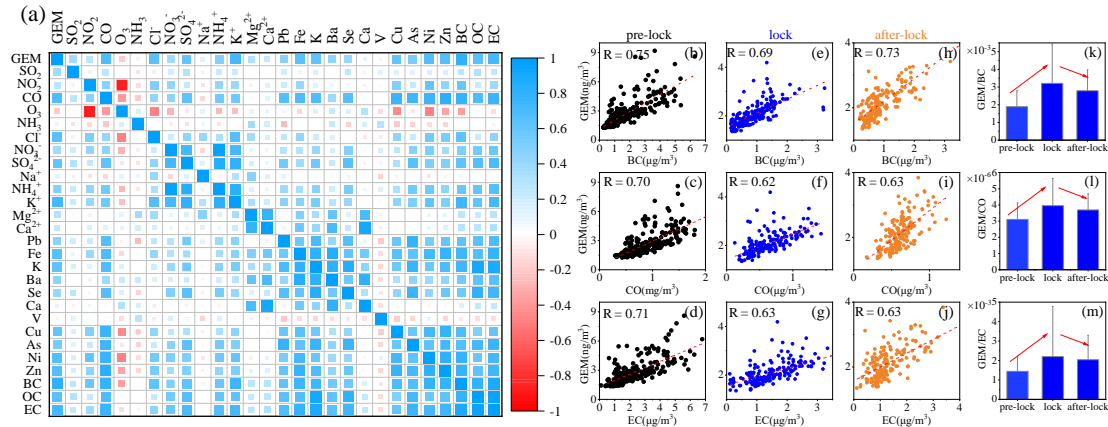

Figure 2. (a) Correlation coefficient matrix among GEM and PM$_{2.5}$ components and gaseous pollutants during the whole study period. Relationship between GEM and BC, CO, and EC (b-d) before, (e-g) during, and (h-j) after the lockdown. (k-m) The change of GEM/BC, GEM/CO, and GEM/EC ratios before, during, and after the lockdown.

Previous studies have demonstrated the strong dependence of natural surface emissions on meteorological factors such as temperature, wind speed, and relative humidity (Pannu et al., 2014; Lindberg et al., 2007; Gustin et al., 2005). We compared the relationship between GEM and meteorological parameters before, during, and after the lockdown to investigate the changes in natural sources of mercury. As shown in Figure 3a-c, there was no clear correlation between GEM and temperature before the lockdown while moderately high correlations during and after the lockdown emerged with the correlation coefficients (R^2) of 0.43 and 0.71, respectively. This might indicate the enhanced role of natural sources on GEM concentrations due to the lockdown control measures. For wind speed (Figure 3d-f), strongly negative correlations were observed with GEM before and after the lockdown, but not during the lockdown. On the one hand, high wind speed was beneficial to the diffusion of air pollutants in the atmosphere, which explained the negative correlation between GEM and wind speed. On the other hand, high wind speed promoted the natural surface release of mercury, partially canceling out the diffusion effect of wind speed, which induced the ambiguous relationship between GEM and wind speed during the lockdown. The relationship between GEM and PBL height was similar to that of wind speed, showing strongly negative

correlations before and after the lockdown while weak correlations during the lockdown (Figure 3g-i). The increase of PBL height was beneficial to the diffusion of GEM. While the increase of PBL height usually occurred in daytime when temperature was high, which was conducive to the natural surface release of mercury. Therefore, ambient GEM did not decrease significantly with the increase of PBL height during the lockdown.

Overall, all the observational evidences possibly suggested that the role of natural emissions on GEM was more manifested due to the lockdown. However, all the results were based on qualitative data analysis. In the following sections, the machine learning and source apportionment methods will be applied to quantify the contribution of anthropogenic and natural sources to GEM during the three defined periods.
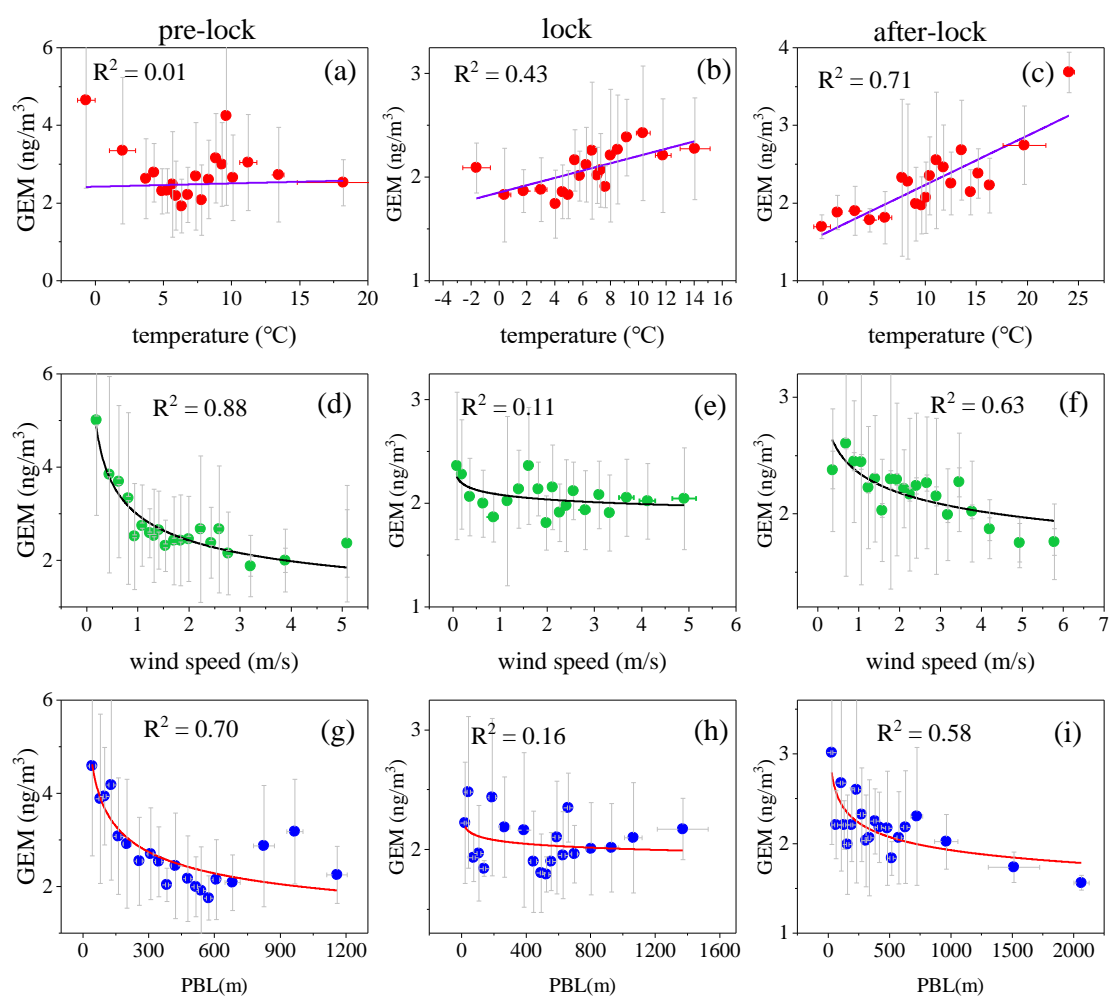
Figure 3. Relationship between GEM concentration and (a-c) temperature, (d-f) wind speed, and (g-i) PBL height before, during, and after the lockdown.

3.3 Understanding the Drivers of GEM Variation by Explainable Machine Learning

We further conducted machine learning simulations using the trained artificial neural network (ANN), which has already been established by training the long-term (2015 - 2019) observational data of GEM and other necessary environmental parameters (including SO_2, NO_2, CO, O_3, $PM_{2.5}$, temperature, relative humidity, and wind speed) at the Dianshan Lake site (Qin et al., 2022). Figure 4a-b shows the comparison of ANN-simulated and observed GEM concentrations during the whole study period, and found their correlation coefficient is acceptable ($R^2 = 0.67$). As shown in Figure S5, we examined the performance of the ANN model before, during, and after the lockdown. The correlations between ANN simulated and observed GEM concentrations were also acceptable with correlation coefficient of 0.67, 0.59, and 0.63, respectively. Then we applied the SHapley Additive exPlanation (SHAP) approach to uncover the mystery of the machine learning "black box" model (See methods in Section 2.3). This approach has the potential to quantify the global and local impacts of input features on model predictions (Lundberg and Lee, 2017a), which has been used in various fields (Mangalathu et al., 2020; Hou et al., 2022; Lundberg et al., 2018; Zhong et al., 2021; Wang et al., 2021).

We calculated the SHAP value of each feature to represent the global importance of the feature, which can be used to indicate the general impact of various features across all samples. As shown in Figure 4c, by comparing the average absolute SHAP values, $PM_{2.5}$ ranked as the most important feature, which changed the simulated GEM concentrations by 0.30 ± 0.20 ng/m^3, followed by CO and temperature with the SHAP values of 0.16 ± 0.25 and 0.14 ± 0.09 ng/m^3, respectively. The average values of the remaining factors were less than 0.1 ng/m^3. We further investigated the relationship between the SHAP value of each feature and its concentration. As shown in Figure 4d-f, with the increase of $PM_{2.5}$, CO, and SO_2 concentrations, their corresponding SHAP values increased accordingly. Previous studies have shown that GEM, $PM_{2.5}$, CO, and SO_2 shared common anthropogenic sources such as the combustion of fossil fuels and biomass (Chong et al., 2019; Fu et al., 2015), thus interpreting the positive effect of various anthropogenic emission sources on GEM. Similar relationship was also found for temperature and relative humidity with their corresponding SHAP values (Figure 4g-h). Since temperature and relative humidity are important factors affecting the natural release of GEM from natural surfaces (Pannu et al., 2014; Wang et al., 2016), the positive

influence of natural surface emissions on GEM was expected. In contrast, the SHAP value of wind speed negatively correlated with the magnitude of wind speed (Figure 4i), indicating the diffusion/accumulation effect of wind speed on GEM. The SHAP values of NO_2 and O_3 did not show obvious correlations with their concentrations (Figure 4j-k). One of the main sources of NO_2 was vehicle emission, which contributed little to GEM. As for O_3, its oxidation on GEM was also limited. Thus, neither NO_2 or O_3 exhibited considerable effects on regulating the GEM variation.
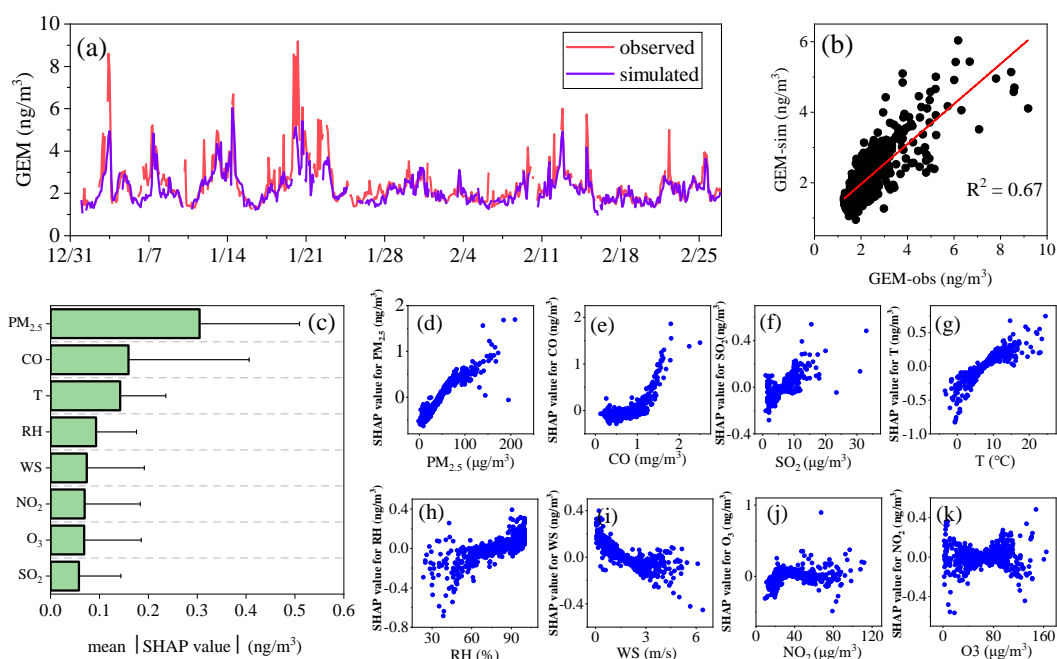
Figure 4. (a) Time-series of observed and ANN-simulated GEM concentrations during the study period. (b) Linear correlation between observed and ANN-simulated GEM concentrations. (c) The ranking of input features calculated via the SHAP algorithm (d-k) Relationship between SHAP value and corresponding concentration of each feature.

To more explicitly identify the drivers to the dynamic variation of GEM, process analysis of GEM pollution episodes was conducted. One pollution episode was defined as its average GEM concentration more than 35% of the day before the episode and lasted for more than three days. Based on this criterion, two pollution episodes (PE1 and PE2) before the lockdown, one pollution episode (PE3) during the lockdown, and one pollution episode (PE4) after the lockdown were selected (Figure S6). As shown in Figure 5, the drivers of the first two pollution episodes were significantly different from the last two. The main influencing factors in PE1 were $PM_{2.5}$ and CO, which represented anthropogenic sources, contributing 0.65 and 0.51 ng/m^3 to the GEM variation,

15

respectively. Similar to PE1, PM$_{2.5}$ and CO in PE2 contributed the most to the GEM variation of 0.35 and 0.12 ng/m^3, respectively. This indicated that the two mercury pollution episodes before the lockdown were mainly driven by anthropogenic sources. In contrast, in PE3 and PE4, temperature ranked the first among all the variables, with contribution to GEM of 0.10 and 0.14 ng/m^3, respectively. This suggested that these two pollution episodes during and after the lockdown occurred under the dominance of natural sources.

In addition, we found that there was a trade-off between the SHAP value of temperature and the SHAP value of PM$_{2.5}$ and CO. As shown in Figure 5b-c, the SHAP value of temperature decreased with the increase of the SHAP value of PM$_{2.5}$ and CO throughout the study period. This probably suggested that the increase of anthropogenic GEM emissions may inhibit the release of natural sources to some extents, which will be discussed later.
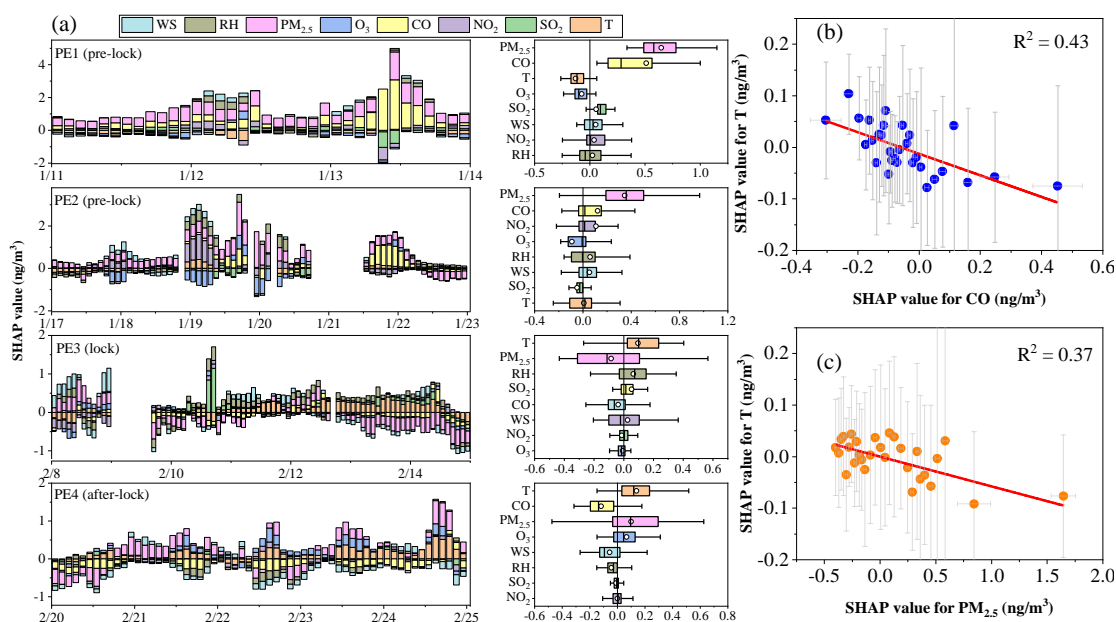

Figure 5. (a) Time series and box plots of each feature's SHAP value during the four mercury pollution episodes (b-c) Relationship between SHAP value of temperature and SHAP value of CO and PM$_{2.5}$ during the whole study period

3.4 Response of Natural Release of GEM to the Lockdown

417   To quantify the changes in the contribution of different sources to GEM, we applied the PMF model

418   to analyze the sources of GEM during the whole study period. Figure S7 shows the resolved factors

419   and factor loadings, which were similar to the results by previous study at the same site (Qin et al.,

420   2020). A total of six sources were resolved, namely coal combustion with high loadings of SO_4^{2-},

421   Pb, K^+, As, and Se, natural surface emissions with high loadings of temperature and NH_3, vehicle

422   emission with high loadings of NO, ship emission with high loading of Ni, iron and steel production

423   with high loadings of Fe, Cr, and Mn, and cement production with high loading of Ca. The mean

424   contributions of the six factors above to GEM were 55%, 28%, 7%, 5%, 3%, and 3%, respectively

425   (Figure S7). To evaluate the uncertainty of the PMF results, the Fpeak model run at the strength of

426   0.5, -0.5, 1, and -1 were conducted by using the rotation tools in PMF. The changes of Q value (dQ)

427   due to the Fpeak rotation were less than 1% of the base run Q (robust) value (Table S3), less than

428   the benchmark value of 5%. The profiles and contributions of each source were also examined, and

429   there were no significant differences between the factor contributions of base run and rotation results,

430   especially for coal combustion and natural surface emission. Hence, the base run results were used

431   in this study.

432   Figure 6a shows the time-series of apportioned GEM concentrations and relative contributions

433   from six sources during three periods. Significant changes in the sources of GEM were observed

434   due to the lockdown. The contribution of coal combustion fell from 60% before the lockdown to

435   51% during the lockdown and 48% after the lockdown. On the opposite, the relative contribution of

436   natural surface emissions rose significantly from 20% before the lockdown to 39% during the

437   lockdown, and then dropped slightly to 33% after the lockdown. In addition to the increased relative

438   contribution of natural surface emissions, its absolute contribution to GEM concentration increased

439   significantly from 0.55 ng/m^3 before the lockdown to 0.80 ng/m^3 during the lockdown, i.e., a 44%

440   increase (Figure 6b). Considering that the synoptic conditions varied little before and during the

441   lockdown, both increases in the absolute and relative contribution of natural surface emissions to

442   GEM during the lockdown should be stimulated by the significant reduction of anthropogenic

443   mercury emissions. Indeed, Figure 6c shows that the absolute contribution of natural surface

444   emissions to GEM and the contribution of anthropogenic sources exhibited a significant negative

445   correlation throughout the study period ($R^2 = 0.86$). This indicated that the significant reduction of

anthropogenic emissions would lead to a significant decrease in the GEM concentration, thereby

disrupting the exchange balance of mercury between the natural surfaces (including soil, vegetation,

and water bodies, etc.) and the atmosphere, resulting in an increase of natural surface release to

compensate for the decrease of GEM concentration in the atmosphere.
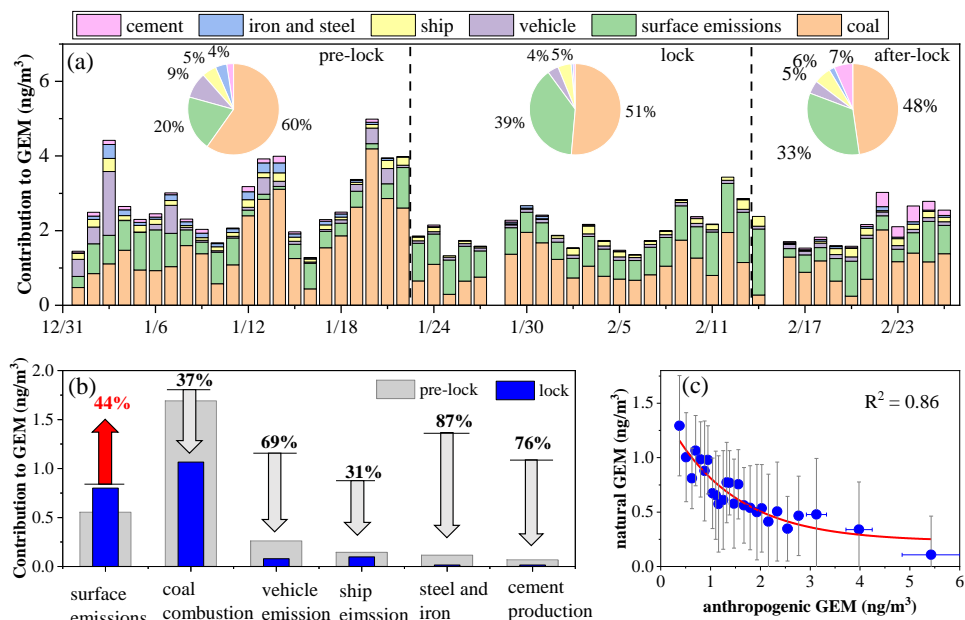
Figure 6. (a) Daily average concentrations of apportioned GEM from six sources based on PMF

modeling. Pie charts represent the relative contribution of the six sources to GEM during three

periods (b) Changes of absolute contribution of natural and anthropogenic sources to GEM before

and during the lockdown (c) Relationship between absolute contribution of natural surface

emissions and anthropogenic sources to GEM during the whole study period

4 Conclusions and Implications

In this work, we investigated the changes of the impact of anthropogenic and natural sources on

GEM in the suburbs of eastern China in the early 2020. Due to the COVID-19 lockdown, GEM was

significantly reduced by 0.72 ng/m^3 compared to that before the lockdown. However, the reduction

extent of GEM was not as strong as most of the other gaseous pollutants (NO_2 and CO) and primary

aerosol species (EC, BC, Pb, and As). Before the lockdown when anthropogenic emissions

dominated, GEM showed no correlation with temperature and negative correlations with wind speed

and the height of PBL. In contrast, GEM showed significant correlation with temperature while the

466   relationship between GEM and wind speed/PBL disappeared during the lockdown, suggesting the

467   enhanced natural emissions of mercury. By applying a machine learning model, GEM was well

468   simulated and the results were interpreted by the Shapley Additive ExPlanation Approach. It was

469   found that the mercury pollution episodes before the lockdown were driven by anthropogenic

470   sources, while they were mainly driven by natural sources during and after the lockdown. Source

471   apportionment results showed that the relative contribution of natural sources to GEM during the

472   lockdown reached 39%, which was significantly higher than that before the lockdown (20%). The

473   absolute contribution of natural sources to GEM during the lockdown was about 0.80 ng/m^3, 44%

474   higher than that before the lockdown. Finally, we revealed the negative correlation between the

475   absolute contribution of natural sources and anthropogenic sources, suggesting the natural release

476   of mercury could be enhanced in response to the significant reduction of anthropogenic mercury

477   emissions.

478   In the long-term, the surface ambient mercury concentration in the northern hemisphere decreased

479   by 30-40% from 1990 to 2010 (Slemr et al., 2011; Soerensen et al., 2012; Cole et al., 2014). From

480   2013 to 2017, the gaseous total mercury concentration in China decreased by about 12% (Liu et al.,

481   2019). It has been long recognized mitigation of anthropogenic mercury emissions regulated this

482   global or regional trend, while the role of natural mercury emissions is less known. Specifically, the

483   response of natural mercury release to the reduction of ambient Hg^0 concentration is ambiguous,

484   which limits better understanding the role of natural sources in global mercury cycling. In this study,

485   the COVID-19 lockdown provided a natural experiment on assessing the dynamic behavior of

486   natural and anthropogenic contributions to gaseous elementary mercury by different means. As

487   shown in Figure S8, the sum of the SHAP values of CO and PM$_{2.5}$ exhibited a good positive

488   correlation with the concentration of GEM contributed by anthropogenic sources based on PMF

489   modeling (R^2 = 0.72). Moderate correlation was also derived between the SHAP value of

490   temperature and the concentration of GEM contributed by natural sources (R^2 = 0.50). This indicated

491   that the results of machine learning with an explainable approach and the traditional receptor model

492   were consistent and corroborated each other. This study highlighted that machine learning coupled

493   with reliable interpretation methods can well quantify the role of different factors in the process of

494   air pollution, showing great potential in the fields of atmospheric science. However, we realize that

the performance of machine learning in simulating atmospheric mercury in this study has yet to be improved. Continuous long-term observations of atmospheric mercury with more monitoring sites are desired to ensure a more adequate training dataset. Also, more relevant environment parameters for GEM are needed to further improve the training performance of machine learning model. In addition, different machine learning methods such as artificial neural network, decision tree, random forest, and Bayesian learning should be evaluated to choose an optimal solution.

The natural release of mercury mainly comes from the exchange between the natural surfaces and the atmosphere, including two processes: (1) the formation of volatile Hg^0 in the surface and (2) the mass transfer of Hg^0 between the interfaces (Zhu et al., 2016). At locations with high ambient Hg^0 concentrations (e.g., mining areas and landfills), the exchange of mercury between the surface and the atmosphere is always dominated by deposition, regardless changes in meteorological conditions (Bash and Miller, 2007; Wang et al., 2007; Zhu et al., 2013). Fluctuations in ambient Hg^0 concentrations can change the Hg^0 concentration gradient at the interfaces and thus affect the Hg^0 exchange flux (Xin and Gustin, 2007). The results of this study imply that the declining in global anthropogenic mercury emissions could stimulate increases in natural surface releases, which may pose challenges to future control of atmospheric mercury pollution.

Data Availability Statement

All data has been uploaded to Zendo (https://doi.org/10.5281/zenodo.6654670).

Author contributions

XQ, CD, and KH designed this study. XQ and SZ performed measurements and data analysis.

XW, QF, JC, YL, YD, and JH performed data collection. XQ and KH wrote the paper.

All have commented on and reviewed the paper.

Competing interests

The authors declare that they have no conflict of interest.

525   42175119, 21777029, 91644105).

526

527   **References**

528   Aas, K., Jullum, M., and Loland, A.: Explaining individual predictions when features are dependent:
529   More accurate approximations to Shapley values, Artificial Intelligence, 298,
530   10.1016/j.artint.2021.103502, 2021.

531   Bahlmann, E., Ebinghaus, R., and Ruck, W.: Development and application of a laboratory flux
532   measurement system (LFMS) for the investigation of the kinetics of mercury emissions from soils,
533   Journal of Environmental Management, 81, 114-125, 10.1016/j.jenvman.2005.09.022, 2006.

534   Bash, J. O. and Miller, D. R.: A note on elevated total gaseous mercury concentrations downwind
535   from an agriculture field during tilling, Sci. Total Environ., 388, 379-388,
536   10.1016/j.scitotenv.2007.07.012, 2007.

537   Belis, C. A., Karagulian, F., Larsen, B. R., and Hopke, P. K.: Critical review and meta-analysis of
538   ambient particulate matter source apportionment using receptor models in Europe, Atmospheric
539   Environment, 69, 94-108, 10.1016/j.atmosenv.2012.11.009, 2013.

540   Carpi, A. and Lindberg, S. E.: Sunlight-mediated emission of elemental mercury from soil amended
541   with municipal sewage sludge, Environmental science & technology, 31, 2085-2091,
542   10.1021/es960910+, 1997.

543   Carpi, A., Fostier, A. H., Orta, O. R., dos Santos, J. C., and Gittings, M.: Gaseous mercury emissions
544   from soil following forest loss and land use changes: Field experiments in the United States and
545   Brazil, Atmospheric Environment, 96, 423-429, 10.1016/j.atmosenv.2014.08.004, 2014.

546   Chang, Y., Huang, R. J., Ge, X., Huang, X., Hu, J., Duan, Y., Zou, Z., Liu, X., and Lehmann, M. F.:
547   Puzzling haze events in China during the coronavirus (COVID-19) shutdown, Geophys Res Lett,
548   e2020GL088533, 10.1029/2020GL088533, 2020.

549   Chang, Y. H., Huang, K., Xie, M. J., Deng, C. R., Zou, Z., Liu, S. D., and Zhang, Y. L.: First long-term
550   and near real-time measurement of trace elements in China's urban atmosphere: temporal
551   variability, source apportionment and precipitation effect, Atmospheric Chemistry and Physics, 18,
552   11793-11812, 10.5194/acp-18-11793-2018, 2018.

553   Chong, X., Wang, Y., Liu, R., Zhang, Y., Zhang, Y., and Zheng, W.: Pollution characteristics and
554   source difference of gaseous elemental mercury between haze and non-haze days in winter, The
555   Science of the total environment, 678, 671-680, 10.1016/j.scitotenv.2019.04.338, 2019.

556   Cole, A. S., Steffen, A., Eckley, C. S., Narayan, J., Pilote, M., Tordon, R., Graydon, J. A., St Louis, V. L.,
557   Xu, X., and Branfireun, B. A.: A Survey of Mercury in Air and Precipitation across Canada: Patterns
558   and Trends, Atmosphere, 5, 635-668, 10.3390/atmos5030635, 2014.

559   Custodio, D., Ebinghaus, R., Spain, T. G., and Bieser, J.: Source apportionment of atmospheric
560   mercury in the remote marine atmosphere: Mace Head GAW station, Irish western coast,
561   Atmospheric Chemistry and Physics, 20, 7929-7939, 10.5194/acp-20-7929-2020, 2020.

562   Driscoll, C. T., Mason, R. P., Chan, H. M., Jacob, D. J., and Pirrone, N.: Mercury as a global pollutant:
563   sources, pathways, and effects, Environmental science & technology, 47, 4967-4983,
564   10.1021/es305071v, 2013.

565   Fu, X. W., Zhang, H., Lin, C. J., Feng, X. B., Zhou, L. X., and Fang, S. X.: Correlation slopes of GEM /
566   CO, GEM / CO_2, and GEM / CH_4 and estimated mercury emissions in
567   China, South Asia, the Indochinese Peninsula, and Central Asia derived from observations in

568 northwestern and southwestern China, Atmos. Chem. Phys., 15, 1013-1028, 10.5194/acp-15-
569 1013-2015, 2015.

570 Giang, A. and Selin, N. E.: Benefits of mercury controls for the United States, Proceedings of the
571 National Academy of Sciences of the United States of America, 113, 286-291,
572 10.1073/pnas.1514395113, 2016.

573 Gibson, M. D., Haelssig, J., Pierce, J. R., Parrington, M., Franklin, J. E., Hopper, J. T., Li, Z., and Ward,
574 T. J.: A comparison of four receptor models used to quantify the boreal wildfire smoke contribution
575 to surface PM$_{2.5}$ in Halifax, Nova Scotia during the BORTAS-B experiment, Atmos.
576 Chem. Phys., 15, 815-827, 10.5194/acp-15-815-2015, 2015.

577 Grange, S. K., Carslaw, D. C., Lewis, A. C., Boleti, E., and Hueglin, C.: Random forest meteorological
578 normalisation models for Swiss PM10 trend analysis, Atmos. Chem. Phys., 18, 6223-6239,
579 10.5194/acp-18-6223-2018, 2018.

580 Gustin, M. S., Engle, M., Ericksen, J., Xin, M., Krabbenhoft, D., Lindberg, S., Olund, S., and Rytuba,
581 J.: New insights into mercury exchange between air and substrate, Geochimica Et Cosmochimica
582 Acta, 69, A700-A700, 2005.

583 Holmes, C. D., Jacob, D. J., Corbitt, E. S., Mao, J., Yang, X., Talbot, R., and Slemr, F.: Global
584 atmospheric model for mercury including oxidation by bromine atoms, Atmos. Chem. Phys., 10,
585 12037-12057, 10.5194/acp-10-12037-2010, 2010.

586 Hopke, P. K.: Review of receptor modeling methods for source apportionment, Journal of the Air
587 & Waste Management Association, 66, 237-259, 10.1080/10962247.2016.1140693, 2016.

588 Horowitz, H. M., Jacob, D. J., Zhang, Y., Dibble, T. S., Slemr, F., Amos, H. M., Schmidt, J. A., Corbitt,
589 E. S., Marais, E. A., and Sunderland, E. M.: A new mechanism for atmospheric mercury redox
590 chemistry: implications for the global mercury budget, Atmospheric Chemistry and Physics, 17,
591 6353-6371, 10.5194/acp-17-6353-2017, 2017.

592 Hou, L., Dai, Q., Song, C., Liu, B., Guo, F., Dai, T., Li, L., Liu, B., Bi, X., Zhang, Y., and Feng, Y.: Revealing
593 Drivers of Haze Pollution by Explainable Machine Learning, Environmental Science & Technology
594 Letters, 9, 112-119, 10.1021/acs.estlett.1c00865, 2022.

595 Huang, S. and Zhang, Y.: Interannual Variability of Air-Sea Exchange of Mercury in the Global
596 Ocean: The "Seesaw Effect" in the Equatorial Pacific and Contributions to the Atmosphere,
597 Environmental science & technology, 55, 7145-7156, 10.1021/acs.est.1c00691, 2021.

598 Huang, X., Ding, A., Gao, J., Zheng, B., Zhou, D., Qi, X., Tang, R., Wang, J., Ren, C., Nie, W., Chi, X.,
599 Xu, Z., Chen, L., Li, Y., Che, F., Pang, N., Wang, H., Tong, D., Qin, W., Cheng, W., Liu, W., Fu, Q., Liu,
600 B., Chai, F., Davis, S. J., Zhang, Q., and He, K.: Enhanced secondary pollution offset reduction of
601 primary emissions during COVID-19 lockdown in China, Natl Sci Rev, 8, nwaa137,
602 10.1093/nsr/nwaa137, 2021.

603 Jiskra, M., Sonke, J. E., Obrist, D., Bieser, J., Ebinghaus, R., Myhre, C. L., Pfaffhuber, K. A., Wangberg,
604 I., Kyllonen, K., Worthy, D., Martin, L. G., Labuschagne, C., Mkololo, T., Ramonet, M., Magand, O.,
605 and Dommergue, A.: A vegetation control on seasonal variations in global atmospheric mercury
606 concentrations, Nat. Geosci., 11, 244-+, 10.1038/s41561-018-0078-8, 2018.

607 Kumar, I. E., Venkatasubramanian, S., Scheidegger, C., and Friedler, S. A.: Problems with Shapley-
608 value-based explanations as feature importance measures, International Conference on Machine
609 Learning (ICML), Electr Network, 2020
610 Jul 13-18, WOS:000683178505057, 2020.

611 Li, H., Huang, K., Fu, Q., Lin, Y., Chen, J., Deng, C., Tian, X., Tang, Q., Song, Q., and Wei, Z.: Airborne

612 black carbon variations during the COVID-19 lockdown in the Yangtze River Delta megacities
613 suggest actions to curb global warming, Environ Chem Lett, 1-10, 10.1007/s10311-021-01327-3,
614 2021.
615 Lindberg, S., Bullock, R., Ebinghaus, R., Engstrom, D., Feng, X. B., Fitzgerald, W., Pirrone, N., Prestbo,
616 E., and Seigneur, C.: A synthesis of progress and uncertainties in attributing the sources of mercury
617 in deposition, Ambio, 36, 19-32, 2007.
618 Liu, K., Wang, S., Wu, Q., Wang, L., Ma, Q., Zhang, L., Li, G., Tian, H., Duan, L., and Hao, J.: A Highly
619 Resolved Mercury Emission Inventory of Chinese Coal-Fired Power Plants, Environmental science
620 & technology, 52, 2400-2408, 10.1021/acs.est.7b06209, 2018.
621 Liu, K., Wu, Q., Wang, L., Wang, S., Liu, T., Ding, D., Tang, Y., Li, G., Tian, H., Duan, L., Wang, X., Fu,
622 X., Feng, X., and Hao, J.: Measure-Specific Effectiveness of Air Pollution Control on China's
623 Atmospheric Mercury Concentration and Deposition during 2013-2017, Environmental science &
624 technology, 10.1021/acs.est.9b02428, 2019.
625 Lundberg, S. M. and Lee, S.-I.: A Unified Approach to Interpreting Model Predictions, 31st Annual
626 Conference on Neural Information Processing Systems (NIPS), Long Beach, CA, 2017
627 Dec 04-09, WOS:000452649404081, 2017.
628 Lundberg, S. M. and Lee, S. I.: A Unified Approach to Interpreting Model Predictions, 31st Annual
629 Conference on Neural Information Processing Systems (NIPS), Long Beach, CA, Dec 04-09,
630 WOS:000452649404081, 2017.
631 Lundberg, S. M., Erion, G., Chen, H., DeGrave, A., Prutkin, J. M., Nair, B., Katz, R., Himmelfarb, J.,
632 Bansal, N., and Lee, S. I.: From Local Explanations to Global Understanding with Explainable AI for
633 Trees, Nat Mach Intell, 2, 56-67, 10.1038/s42256-019-0138-9, 2020.
634 Lundberg, S. M., Nair, B., Vavilala, M. S., Horibe, M., Eisses, M. J., Adams, T., Liston, D. E., Low, D.
635 K.-W., Newman, S.-F., Kim, J., and Lee, S.-I.: Explainable machine-learning predictions for the
636 prevention of hypoxaemia during surgery, Nature Biomedical Engineering, 2, 749-760,
637 10.1038/s41551-018-0304-0, 2018.
638 Mangalathu, S., Hwang, S.-H., and Jeon, J.-S.: Failure mode and effects analysis of RC members
639 based on machine-learning-based SHapley Additive exPlanations (SHAP) approach, Engineering
640 Structures, 219, 110927, https://doi.org/10.1016/j.engstruct.2020.110927, 2020.
641 Mao, H., Cheng, I., and Zhang, L.: Current understanding of the driving mechanisms for
642 spatiotemporal variations of atmospheric speciated mercury: a review, Atmos. Chem. Phys., 16,
643 12897-12924, 10.5194/acp-16-12897-2016, 2016.
644 Mazur, M., Mitchell, C. P. J., Eckley, C. S., Eggert, S. L., Kolka, R. K., Sebestyen, S. D., and Swain, E.
645 B.: Gaseous mercury fluxes from forest soils in response to forest harvesting intensity: A field
646 manipulation experiment, Sci. Total Environ., 496, 678-687, 10.1016/j.scitotenv.2014.06.058, 2014.
647 Moore, C. and Carpi, A.: Mechanisms of the emission of mercury from soil: Role of UV radiation, J.
648 Geophys. Res.-Atmos., 110, 10.1029/2004jd005567, 2005.
649 Obrist, D., Kirk, J. L., Zhang, L., Sunderland, E. M., Jiskra, M., and Selin, N. E.: A review of global
650 environmental mercury processes in response to human and natural perturbations: Changes of
651 emissions, climate, and land use, Ambio, 47, 116-140, 10.1007/s13280-017-1004-9, 2018.
652 Outridge, P. M., Mason, R. P., Wang, F., Guerrero, S., and Heimbürger-Boavida, L. E.: Updated
653 Global and Oceanic Mercury Budgets for the United Nations Global Mercury Assessment 2018,
654 Environmental science & technology, 52, 11466-11477, 10.1021/acs.est.8b01246, 2018.
655 Pannu, R., Siciliano, S. D., and O'Driscoll, N. J.: Quantifying the effects of soil temperature, moisture

656 and sterilization on elemental mercury formation in boreal soils, Environmental Pollution, 193,
657 138-146, 10.1016/j.envpol.2014.06.023, 2014.

658 Pirrone, N., Cinnirella, S., Feng, X., Finkelman, R. B., Friedli, H. R., Leaner, J., Mason, R., Mukherjee,
659 A. B., Stracher, G. B., Streets, D. G., and Telmer, K.: Global mercury emissions to the atmosphere
660 from anthropogenic and natural sources, Atmos. Chem. Phys., 10, 5951-5964, 10.5194/acp-10-
661 5951-2010, 2010.

662 Poissant, L., Pilote, M., Constant, P., Beauvais, C., Zhang, H. H., and Xu, X. H.: Mercury gas
663 exchanges over selected bare soil and flooded sites in the bay St. Francois wetlands (Quebec,
664 Canada), Atmospheric Environment, 38, 4205-4214, 10.1016/j.atmosenv.2004.03.068, 2004.

665 Qi, Y., Li, Q., Karimian, H., and Liu, D.: A hybrid model for spatiotemporal forecasting of PM2.5
666 based on graph convolutional neural network and long short-term memory, The Science of the
667 total environment, 664, 1-10, 10.1016/j.scitotenv.2019.01.333, 2019.

668 Qin, X., Wang, X., Shi, Y., Yu, G., Zhao, N., Lin, Y., Fu, Q., Wang, D., Xie, Z., Deng, C., and Huang, K.:
669 Characteristics of atmospheric mercury in a suburban area of east China: sources, formation
670 mechanisms, and regional transport, Atmos. Chem. Phys., 19, 5923-5940, 10.5194/acp-19-5923-
671 2019, 2019.

672 Qin, X., Zhou, S., Li, H., Wang, G., Wang, X., Fu, Q., Duan, Y., Lin, Y., Huo, J., Huang, K., and Deng,
673 C.: Simulation of Spatiotemporal Trends of Gaseous Elemental Mercury in the Yangtze River Delta
674 of Eastern China by an Artificial Neural Network, Environmental Science & Technology Letters,
675 10.1021/acs.estlett.1c01025, 2022.

676 Qin, X., Zhang, L., Wang, G., Wang, X., Fu, Q., Xu, J., Li, H., Chen, J., Zhao, Q., Lin, Y., Huo, J., Wang,
677 F., Huang, K., and Deng, C.: Assessing contributions of natural surface and anthropogenic
678 emissions to atmospheric mercury in a fast-developing region of eastern China from 2015 to 2018,
679 Atmos. Chem. Phys., 20, 10985-10996, 10.5194/acp-20-10985-2020, 2020.

680 Selin, N. E., Jacob, D. J., Park, R. J., Yantosca, R. M., Strode, S., Jaegle, L., and Jaffe, D.: Chemical
681 cycling and deposition of atmospheric mercury: Global constraints from observations, J. Geophys.
682 Res.-Atmos., 112, 10.1029/2006jd007450, 2007.

683 Slemr, F., Brunke, E. G., Ebinghaus, R., and Kuss, J.: Worldwide trend of atmospheric mercury since
684 1995, Atmospheric Chemistry and Physics, 11, 4779-4787, 10.5194/acp-11-4779-2011, 2011.

685 Soerensen, A. L., Jacob, D. J., Streets, D. G., Witt, M. L. I., Ebinghaus, R., Mason, R. P., Andersson,
686 M., and Sunderland, E. M.: Multi-decadal decline of mercury in the North Atlantic atmosphere
687 explained by changing subsurface seawater concentrations, Geophys. Res. Lett., 39,
688 10.1029/2012gl053736, 2012.

689 Steenhuisen, F. and Wilson, S. J.: Development and application of an updated geospatial
690 distribution model for gridding 2015 global mercury emissions, Atmospheric Environment, 211,
691 138-150, https://doi.org/10.1016/j.atmosenv.2019.05.003, 2019.

692 Stirnberg, R., Cermak, J., Kotthaus, S., Haeffelin, M., Andersen, H., Fuchs, J., Kim, M., Petit, J. E., and
693 Favez, O.: Meteorology-driven variability of air pollution (PM1) revealed with explainable machine
694 learning, Atmos. Chem. Phys., 21, 3919-3948, 10.5194/acp-21-3919-2021, 2021.

695 Streets, D. G., Devane, M. K., Lu, Z. F., Bond, T. C., Sunderland, E. M., and Jacob, D. J.: All-Time
696 Releases of Mercury to the Atmosphere from Human Activities, Environmental science &
697 technology, 45, 10485-10491, 10.1021/es202765m, 2011.

698 Streets, D. G., Horowitz, H. M., Lu, Z., Levin, L., Thackray, C. P., and Sunderland, E. M.: Global and
699 regional trends in mercury emissions and concentrations, 2010–2015, Atmospheric Environment,

201, 417-427, 10.1016/j.atmosenv.2018.12.031, 2019.

Sun, Y., Chen, C., Zhang, Y., Xu, W., Zhou, L., Cheng, X., Zheng, H., Ji, D., Li, J., Tang, X., Fu, P., and Wang, Z.: Rapid formation and evolution of an extreme haze episode in Northern China during winter 2015, Scientific reports, 6, 27151, 10.1038/srep27151, 2016.

Tang, Y., Wang, S. X., Wu, Q. R., Liu, K. Y., Wang, L., Li, S., Gao, W., Zhang, L., Zheng, H. T., Li, Z. J., and Hao, J. M.: Recent decrease trend of atmospheric mercury concentrations in East China: the influence of anthropogenic emissions, Atmospheric Chemistry and Physics, 18, 8279-8291, 10.5194/acp-18-8279-2018, 2018.

Vu, T. V., Shi, Z., Cheng, J., Zhang, Q., He, K., Wang, S., and Harrison, R. M.: Assessing the impact of clean air action on air quality trends in Beijing using a machine learning technique, Atmos. Chem. Phys., 19, 11303-11314, 10.5194/acp-19-11303-2019, 2019.

Wang, C., Feng, L., and Qi, Y.: Explainable deep learning predictions for illness risk of mental disorders in Nanjing, China, Environmental Research, 202, 111740, https://doi.org/10.1016/j.envres.2021.111740, 2021.

Wang, G., Huang, K., Fu, Q., Chen, J., Huo, J., Zhao, Q., Duan, Y., Lin, Y., Yang, F., Zhang, W., Li, H., Xu, J., Qin, X., Zhao, N., and Deng, C.: Response of PM2.5-bound elemental species to emission variations and associated health risk assessment during the COVID-19 pandemic in a coastal megacity, Journal of Environmental Sciences, 122, 115-127, 10.1016/j.jes.2021.10.005, 2022a.

Wang, G. C., Chen, J., Xu, J., Yun, L., Zhang, M. D., Li, H., Qin, X. F., Deng, C. R., Zheng, H. T., Gui, H. Q., Liu, J. G., and Huang, K.: Atmospheric Processing at the Sea-Land Interface Over the South China Sea: Secondary Aerosol Formation, Aerosol Acidity, and Role of Sea Salts, J. Geophys. Res.-Atmos., 127, 10.1029/2021jd036255, 2022b.

Wang, S. F., Feng, X. B., Qiu, G. L., Fu, X. W., and Wei, Z. Q.: Characteristics of mercury exchange flux between soil and air in the heavily air-polluted area, eastern Guizhou, China, Atmospheric Environment, 41, 5584-5594, 10.1016/j.atmosenv.2007.03.002, 2007.

Wang, X., Lin, C. J., and Feng, X.: Sensitivity analysis of an updated bidirectional air-surface exchange model for elemental mercury vapor, Atmospheric Chemistry and Physics, 14, 6273-6287, 10.5194/acp-14-6273-2014, 2014.

Wang, X., Lin, C.-J., Yuan, W., Sommar, J., Zhu, W., and Feng, X.: Emission-dominated gas exchange of elemental mercury vapor over natural
surfaces in China, Atmospheric Chemistry and Physics, 16, 11125-11143, 10.5194/acp-16-11125-2016, 2016.

Wanninkhof, R.: Relationship between wind speed and gas exchange over the ocean revisited, Limnology and Oceanography-Methods, 12, 351-362, 10.4319/lom.2014.12.351, 2014.

Wen, M., Wu, Q., Li, G., Wang, S., Li, Z., Tang, Y., Xu, L., and Liu, T.: Impact of ultra-low emission technology retrofit on the mercury emissions and cross-media transfer in coal-fired power plants, Journal of Hazardous Materials, 396, 10.1016/j.jhazmat.2020.122729, 2020.

Wu, Q., Tang, Y., Wang, L., Wang, S., Han, D., Ouyang, D., Jiang, Y., Xu, P., Xue, Z., and Hu, J.: Impact of emission reductions and meteorology changes on atmospheric mercury concentrations during the COVID-19 lockdown, The Science of the total environment, 750, 142323, 10.1016/j.scitotenv.2020.142323, 2021.

Wu, Q. R., Wang, S. X., Liu, K. Y., Li, G. L., and Hao, J. M.: Emission-Limit-Oriented Strategy To Control Atmospheric Mercury Emissions in Coal-Fired Power Plants toward the Implementation of the Minamata Convention, Environmental science & technology, 52, 11087-11093,

744　10.1021/acs.est.8b02250, 2018.

745　Wu, Q. R., Wang, S. X., Li, G. L., Liang, S., Lin, C. J., Wang, Y. F., Cai, S. Y., Liu, K. Y., and Hao, J. M.:
746　Temporal Trend and Spatial Distribution of Speciated Atmospheric Mercury Emissions in China
747　During 1978-2014, Environmental science & technology, 50, 13428-13435,
748　10.1021/acs.est.6b04308, 2016.

749　Xin, M. and Gustin, M. S.: Gaseous elemental mercury exchange with low mercury containing soils:
750　Investigation of controlling factors, Appl. Geochem., 22, 1451-1466,
751　10.1016/j.apgeochem.2007.02.006, 2007.

752　Xu, J., Wang, Q. Z., Deng, C. R., McNeill, V. F., Fankhauser, A., Wang, F. W., Zheng, X. J., Shen, J. D.,
753　Huang, K., and Zhuang, G. S.: Insights into the characteristics and sources of primary and secondary
754　organic carbon: High time resolution observation in urban Shanghai, Environmental Pollution, 233,
755　1177-1187, 10.1016/j.envpol.2017.10.003, 2018.

756　Xu, J., Chen, J., Shi, Y. J., Zhao, N., Qin, X. F., Yu, G. Y., Liu, J. M., Lin, Y. F., Fu, Q. Y., Weber, R. J., Lee,
757　S. H., Deng, C. R., and Huang, K.: First Continuous Measurement of Gaseous and Particulate Formic
758　Acid in a Suburban Area of East China: Seasonality and Gas-Particle Partitioning, Acs Earth and
759　Space Chemistry, 4, 157-167, 10.1021/acsearthspacechem.9b00210, 2020.

760　Xu, X., Liao, Y., Cheng, I., and Zhang, L.: Potential sources and processes affecting speciated
761　atmospheric mercury at Kejimkujik National Park, Canada: comparison of receptor models and
762　data treatment methods, Atmospheric Chemistry and Physics, 17, 1381-1400, 10.5194/acp-17-
763　1381-2017, 2017.

764　Yang, J., Wen, Y., Wang, Y., Zhang, S., Pinto, J. P., Pennington, E. A., Wang, Z., Wu, Y., Sander, S. P.,
765　Jiang, J. H., Hao, J., Yung, Y. L., and Seinfeld, J. H.: From COVID-19 to future electrification:
766　Assessing traffic impacts on air quality by a machine-learning model, Proc Natl Acad Sci U S A,
767　118, 10.1073/pnas.2102705118, 2021.

768　Yin, X., Kang, S., de Foy, B., Ma, Y., Tong, Y., Zhang, W., Wang, X., Zhang, G., and Zhang, Q.: Multi-
769　year monitoring of atmospheric total gaseous mercury at a remote high-altitude site (Nam Co,
770　4730 m a.s.l.) in the inland Tibetan Plateau region, Atmospheric Chemistry and Physics, 18, 10557-
771　10574, 10.5194/acp-18-10557-2018, 2018.

772　Yu, Y., He, S., Wu, X., Zhang, C., Yao, Y., Liao, H., Wang, Q., and Xie, M.: PM2.5 elements at an urban
773　site in Yangtze River Delta, China: High time-resolved measurement and the application in source
774　apportionment, Environ Pollut, 253, 1089-1099, 10.1016/j.envpol.2019.07.096, 2019.

775　Zhang, L., Wang, S. X., Wang, L., and Hao, J. M.: Atmospheric mercury concentration and chemical
776　speciation at a rural site in Beijing, China: implications of mercury emission sources, Atmospheric
777　Chemistry and Physics, 13, 10505-10516, 10.5194/acp-13-10505-2013, 2013.

778　Zhang, L., Wang, S., Wu, Q., Wang, F., Lin, C. J., Zhang, L., Hui, M., Yang, M., Su, H., and Hao, J.:
779　Mercury transformation and speciation in flue gases from anthropogenic emission sources: a
780　critical review, Atmos. Chem. Phys., 16, 2417-2433, 10.5194/acp-16-2417-2016, 2016a.

781　Zhang, Y., Jacob, D. J., Horowitz, H. M., Chen, L., Amos, H. M., Krabbenhoft, D. P., Slemr, F., St Louis,
782　V. L., and Sunderland, E. M.: Observed decrease in atmospheric mercury explained by global
783　decline in anthropogenic emissions, Proc Natl Acad Sci U S A, 113, 526-531,
784　10.1073/pnas.1516312113, 2016b.

785　Zheng, B., Tong, D., Li, M., Liu, F., Hong, C., Geng, G., Li, H., Li, X., Peng, L., Qi, J., Yan, L., Zhang, Y.,
786　Zhao, H., Zheng, Y., He, K., and Zhang, Q.: Trends in China's anthropogenic emissions since 2010
787　as the consequence of clean air actions, Atmospheric Chemistry and Physics, 18, 14095-14111,

788 10.5194/acp-18-14095-2018, 2018.

789 Zhong, S., Zhang, K., Wang, D., and Zhang, H.: Shedding light on "Black Box" machine learning
790 models for predicting the reactivity of HO radicals toward organic compounds, Chemical
791 Engineering Journal, 405, 126627, https://doi.org/10.1016/j.cej.2020.126627, 2021.

792 Zhu, J., Wang, T., Talbot, R., Mao, H., Hall, C. B., Yang, X., Fu, C., Zhuang, B., Li, S., Han, Y., and
793 Huang, X.: Characteristics of atmospheric Total Gaseous Mercury (TGM) observed in urban Nanjing,
794 China, Atmospheric Chemistry and Physics, 12, 12103-12118, 10.5194/acp-12-12103-2012, 2012.

795 Zhu, W., Lin, C. J., Wang, X., Sommar, J., Fu, X., and Feng, X.: Global observations and modeling of
796 atmosphere–surface exchange of elemental mercury: a critical review, Atmos. Chem. Phys., 16,
797 4451-4480, 10.5194/acp-16-4451-2016, 2016.

798 Zhu, W., Sommar, J., Li, Z., Feng, X., Lin, C.-J., and Li, G.: Highly elevated emission of mercury vapor
799 due to the spontaneous combustion of refuse in a landfill, Atmospheric Environment, 79, 540-545,
800 10.1016/j.atmosenv.2013.07.016, 2013.

801